



**HAL**  
open science

## A parameter to probe microdroplet dynamics and crystal nucleation

R. Grossier, Victoria Tishkova, R. Morin, S. Veessler

► **To cite this version:**

R. Grossier, Victoria Tishkova, R. Morin, S. Veessler. A parameter to probe microdroplet dynamics and crystal nucleation. AIP Advances, 2018, 8, pp.075324. 10.1063/1.5034443 . hal-01744090v1

**HAL Id: hal-01744090**

**<https://hal.science/hal-01744090v1>**

Submitted on 27 Mar 2018 (v1), last revised 24 Aug 2018 (v2)

**HAL** is a multi-disciplinary open access archive for the deposit and dissemination of scientific research documents, whether they are published or not. The documents may come from teaching and research institutions in France or abroad, or from public or private research centers.

L'archive ouverte pluridisciplinaire **HAL**, est destinée au dépôt et à la diffusion de documents scientifiques de niveau recherche, publiés ou non, émanant des établissements d'enseignement et de recherche français ou étrangers, des laboratoires publics ou privés.

# An order parameter to probe microdroplet dynamics

R. Grossier, V. Tishkova, R. Morin, and S. Veessler  
Centre Interdisciplinaire de Nanoscience de Marseille  
CINaM - CNRS, Aix-Marseille Université  
Campus de Luminy, Case 913, F-13288 Marseille Cedex 09, France  
Phone : +336 6292 2866, Fax : +334 9141 8916, [grossier@cinam.univ-mrs.fr](mailto:grossier@cinam.univ-mrs.fr);  
[veessler@cinam.univ-mrs.fr](mailto:veessler@cinam.univ-mrs.fr)

## Abstract:

We present a simple and efficient digital-image processing method to simultaneously monitor the contraction of a statistically relevant number of microdroplets of the same size and the nucleation of single salt crystals inside. Each individual microdroplet image is reduced to a scalar, standard deviation  $\sigma$ , and overall microdroplet dynamics is monitored using standard-deviation time-evolution plots. It is shown that this approach makes it possible to measure the nucleation time and also that microdroplets interact via water diffusion dynamics. This effect actually decreases the nucleation rate, contrary to previous findings. This “ $\sigma$  approach” can be compared to recording the order parameter in phase transition, which makes it ideal for studying dynamics of systems where images are the primary outputs.

Microdroplets ( $\mu$ Ds) are a versatile experimental tool for visualising, characterising or measuring physicochemical properties[1]. They can be studied for themselves to reveal how sensitive to local environment their dynamics are (evaporation, dissolution or contraction)[2-5] or to make phenomena occur at specific locations[6-8] or to perform multiple experiments where statistics are of importance[9]. However, studying the dynamics of a statistically significant number of  $\mu$ Ds requires the analysis of a huge amount of data. Here we probe  $\mu$ D dynamics using 2D ensemble of roughly  $10^3$   $\mu$ Ds of salted water immersed in an oil film and subjected to water evaporation, leading to nucleation of single crystals of salt. Under these conditions, weakly contrasted images are acquired every second for roughly  $10^3$  seconds. The million images thus yielded clearly exceed our aims: to monitor  $\mu$ D dynamics and crystal nucleation time. What we show here is that the state of a  $\mu$ D at a given time  $t$  can simply and efficiently be described by a scalar  $\sigma(t)$ , a quantity easily extracted from an image of this  $\mu$ D at time  $t$ . This scalar is the standard deviation of the grey-level of pixels inside a region of interest (ROI) containing the  $\mu$ D image. This approach makes it possible to measure the nucleation time and also reveals that  $\mu$ Ds interact via water diffusion. Importantly, this effect is shown to decrease the nucleation rate, contrary to previous findings[10]. Although closer to an information model than a physical model, this “ $\sigma$  approach” is similar to recording the order parameter in phase transition. This makes it ideal for studying the dynamics of systems where images are the primary outputs.

Our work can be seen as an extension of the work of Schäfle et al.[11], who presented a simple method to quantify the temporal evolution of an ordered array of  $\mu$ Ds leading to a superlattice through cooperative effects between  $\mu$ Ds. They measured the mean pixel histogram intensity ratio for carefully selected  $\mu$ D pairs at different superlattice sites during evaporation. They observed that under certain conditions the  $\mu$ Ds do not evaporate independently but cooperatively, by matter exchange through the gas phase. However, the method has several limitations. First, ordered arrays of  $\mu$ Ds needs to be prepared using a patterned surface. Second,  $\mu$ Ds needs to be examined in pairs to compare their relative evaporation rate. Third, intensity ratios can only be used to indicate a cooperative process when evaporation rates are clearly

different. Another experimental approach was proposed by Bonn et al.[12] to demonstrate the interaction between a collection of small monodisperse droplets. They used a precision balance to monitor the mass of the evaporating system. While both approaches[11,12] are elegant, they do not provide information on individual  $\mu\text{D}$  contraction. Our approach overcomes many of these limitations.

Here, arrays of sessile  $\mu\text{D}$ s are generated by a microinjector on an oil-covered 18mm-diameter glass coverslip treated so as to obtain a surface preventing  $\mu\text{D}$ s from spreading and coalescing (Fig.S1), as described previously[13] (additional details available in Supplemental Material). Two  $\mu\text{D}$  arrays are presented (Fig.1 and S2), both prepared under the same conditions except for relative humidity % in room atmosphere (RH) above DMS oil and initial  $\mu\text{D}$  radius (R) (see Supplemental Material).

Both  $\mu\text{D}$  generation and subsequent contraction are observed under a transmission optical microscope. We stop imaging when contraction of each  $\mu\text{D}$  has reached completion: all the water in the  $\mu\text{D}$  has diffused through oil and there is a NaCl crystal at each  $\mu\text{D}$  position (Fig. S3). The first image just after  $\mu\text{D}$  generation (Fig. 1) is processed using FIJI software (Image J, NIH, USA). After thresholding and binarisation procedures, we use the “Analyze Particles” plugin to individually detect each  $\mu\text{D}$  position and size. A rectangular ROI is then assigned to each  $\mu\text{D}$  (Figs.1b and S4). From this ROI, comprising a single  $\mu\text{D}$  and its immediate vicinity, we extract the histogram of pixel grey-levels (Fig.1c). We focus on its standard deviation  $\sigma$ , a measure of the homogeneity of pixel grey-levels[14]. As each individual  $\mu\text{D}$  and its immediate vicinity, on each image, is reduced to a single number ( $\sigma$ ),  $\mu\text{D}$  time evolution can be monitored throughout associated ROI standard deviation time evolution (ROI,  $\sigma$ , t), as reported for a single  $\mu\text{D}$  in Fig. 2a. Each (ROI,  $\sigma$ , t)-plot is then processed with home-made PYTHON codes (www.python.org) to extract characteristic points.

The  $\mu\text{D}$  contraction process leading to crystal nucleation was previously described in [15], and is recalled here (Fig.S3 and video S1). Throughout the contraction process, water is leaving the  $\mu\text{D}$ , thus increasing NaCl concentration. This increases the  $\mu\text{D}$  refractive index, which leads to two characteristic stages. First, as the  $\mu\text{D}$  starting refractive index is lower than the DMS index, the  $\mu\text{D}$  refractive index will gradually increase until it matches the DMS refractive index exactly. At this matching time ( $t_M$ ) the  $\mu\text{D}$  optically disappears. Second, as the contraction process proceeds, the  $\mu\text{D}$  refractive index will exceed the DMS refractive index: the  $\mu\text{D}$  gradually reappears until sudden nucleation occurs at nucleation time ( $t_N$ ). Then a single crystal rapidly grows, before the  $\mu\text{D}$  dries completely at drying time ( $t_D$ ).

Taking a single  $\mu\text{D}$  (assumed spherical cap, due to their small size compared to the capillary length, 2.7mm for a water droplet), with a starting concentration of 0.025 of the NaCl saturation value, the volume has to be divided by 40 before saturation concentration is reached. In terms of measurement dynamics,  $\mu\text{D}$  diameter explores one order of magnitude (50.2  $\mu\text{m}$  at generation, 14.9  $\mu\text{m}$  at saturation and in micrometer range at nucleation), volume explores two orders of magnitude (60.7 pL to <1pL), and the resulting crystal is in the micrometre range. Such spatial dynamics make it difficult to apply measurement techniques where spatial resolution is required: image resolution decreases with the number of  $\mu\text{D}$ s simultaneously observed. Considering magnification alone (1.3 $\mu\text{m}$  per pixel here), while some uncertainty on starting diameter is acceptable (2.6 $\mu\text{m}$  for a 50 $\mu\text{m}$  diameter  $\mu\text{D}$ , i.e  $\Delta D/D=5\%$  error), this no longer applies when  $\mu\text{D}$ s reach 14.9 $\mu\text{m}$  diameter. At this point,  $\Delta D/D=17.4\%$ , which, translated into volume, corresponds to an uncertainty of  $\Delta V/V = 52.2\%$ . Moreover, the size of the resulting crystal is similar to the resolution. Added to this spatial resolution issue, the vanishing refractive index difference ( $\Delta n$ ) between continuous phase (here DMS oil) and dispersed phase ( $\mu\text{D}$ s) does not simplify measurements: edge contrast will fade and disappear during part of the contraction process. At a minimum, these limitations prevent the usual optical techniques from

determining  $t_M$  where the  $\mu D$  is both small and optically invisible, and under certain conditions also prevent determination of nucleation time  $t_N$ .

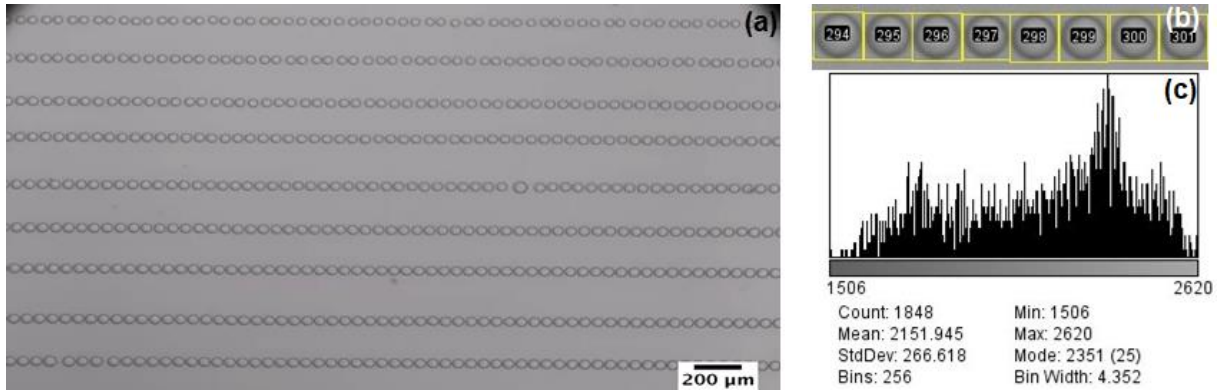


**FIG. 1: Array1** (a) immediately after generation, bottom line (line 9) is the most recently generated, 527  $\mu D$ s with initial droplet radius of  $25.1\mu m \pm 0.8$  (for line 9), with a volume of 60.7pL assuming a contact angle of  $130^\circ$ [16], (b)  $\mu D$ s with the ROI of a magnified area of (a) (line 6 from the top) at  $t=133s$  after the generation of **Array 1** and (c) grey level histogram for the ROI of  $\mu D$  294 at  $t=270s$ .

By reducing  $\mu D$  and its vicinity (the ROI) to a single scalar like  $\sigma$ , we identify the  $\mu D$  signal as any departure from system noise. It is in fact a differential point probe measurement approach similar to signal-to-noise ratio measurement (defined as  $\sigma^2/\mu$ , with  $\mu$  = mean of the signal), except that we only focus on standard deviation of the full grey-level distribution of pixels inside the ROI. At the refractive index matching time,  $t_M$ ,  $\sigma$  is minimum: this is the standard deviation of the noise of our system. Anywhere else (before and after  $t_M$ ), the grey-level distribution of pixels contained in the ROI, and the associated  $\sigma$ , results from the  $\mu D$  contraction process via the interplay between illumination path,  $\mu D$  geometry (diameter, contact angle, height) and difference in refractive index,  $\Delta n$ , with surrounding media. Three populations of pixels and their associated grey-level distribution can be distinguished, each contributing to the signal  $\sigma$  emerging from the ROI. (1) Those in the vicinity of the  $\mu D$ , fixed by the system noise. (2) The brightness decay zone, extending from  $\mu D$  edge toward centre, fixed by  $\Delta n$  and the  $\mu D$  geometry, both determined by Brewster and total internal reflexion angles relative to illumination path. (3)- The central  $\mu D$  area, where light absorption occurs along the direct light path. The balance of pixel grey-level distributions associated with these populations gives rise, throughout  $\mu D$  contraction, to the measured signal and its evolution:  $\sigma$ -curves (Fig.2a).

The variation of  $\sigma$  in the vicinity of  $t_M$  is related to  $\Delta n$ : it decreases before  $t_M$ , and increases afterwards. This makes  $t_M$  a global minimum on the  $\sigma$ -curve, easy to find numerically. At  $t_N$ , the smooth evolution of  $\sigma$  throughout the contraction process is hindered by the nucleation and fast growth of a crystal inside the  $\mu D$ . This clear and sudden jump of  $\sigma$  to higher values is easy to determine with simple thresholding procedures. Then, the nucleated crystal will grow until the  $\mu D$  completely dries,  $t_D$ . Note that precise determination of  $t_D$  requires more sophisticated algorithms than this simple minimum determination and thresholding, and will not be addressed here.

The information obtained here on each individual  $\mu D$  from (ROI,  $\sigma$ , t)-plots is sparse compared to the usual approaches (side-views systems)[16-18] where, with the help of highly resolved images, geometrical  $\mu D$  parameters (diameter, contact diameter, contact angle, height) are monitored. However, our approach overcomes the acknowledged limitations to the study of collective contraction effects[12,17,19], such as the low number of droplets in the patterns (limiting statistical validity) and their large size (possible convection). For instance, for the 527  $\mu D$ s in **Array 1**, we plot in Fig. 2b the  $t_M$  cumulative distribution frequency (CDF). Despite the

monodisperse  $\mu\text{D}$  starting sizes, they do not contract at the same rate, which might appear to be due solely to their different local pinning conditions. However, when  $\mu\text{D}$  position in the array is taken into account in plotting line-by-line  $t_{\text{M}}$ -CDF (Fig. 2c), the main reason for such a wide contraction rate distribution is revealed: collective effects, i.e. neighbour-dependent contraction rates. This results from the instantaneous water concentration field and subsequent gradients a  $\mu\text{D}$  will experience, fixed both by itself and by neighbouring  $\mu\text{D}$ s. Comparing the general trend from one  $\mu\text{D}$  line to another (Fig. 2c), we see high similarity in the shape of their respective CDFs. This results from a spatial scale common to all lines: the  $\mu\text{D}$ -to- $\mu\text{D}$  first-neighbour distance within a line is uniform throughout the array (at generation time). Only local pinning due to impurity will modify this uniformity. The shift in  $t_{\text{M}}$ -CDF mean values for each line comes from another spatial scale, line-to-line distance, by far larger and less uniform than  $\mu\text{D}$ -to- $\mu\text{D}$  first-neighbour distance within a line. External array lines (1 and 9) only have a single neighbouring line (respectively 2 and 8), which explains why they statistically contract faster. For the inner lines, the position of  $t_{\text{M}}$  mean values is a function of its distance from the two neighbouring lines, and line 5 is the most representative of this behaviour: it is the fastest of the inner lines, being the farthest from neighbouring lines.

Interestingly, there is good superimposition of both outer lines (1 and 9) CDFs: despite being generated at different times and different spatial locations on the substrate, they still present the same CDF. This validates the  $\mu\text{D}$  generation method and confirms the homogeneity of the PMMA substrate: while local pinning still occurs, we observe enough  $\mu\text{D}$ s to make it appear as noise on the CDF shape shown by both lines. To resume, the difference between two CDFs comes from differences both in  $\mu\text{D}$  diameters and local pinning, but the statistical approach allows us to identify a common CDF. The plots of **Array 2**  $t_{\text{M}}$ -CDF show the same trends (Figs. S5a and S5b).

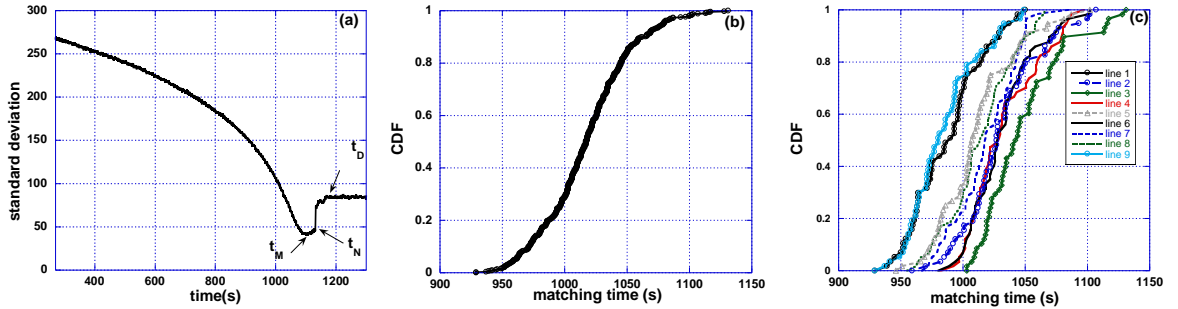


**FIG. 2:** (a) (ROI,  $\sigma$ ,  $t$ )-plot of  $\mu\text{D}\#294$  of **Array 1** (Fig. S4a).  $t_{\text{M}}$ -CDF of **Array 1** (b) for the 527  $\mu\text{D}$ s, and (c) line-by-line, line 1 to line 9 from top to bottom of Fig.1.

Moreover, our approach makes it possible to measure nucleation induction times of each  $\mu\text{D}$  in the array. Nucleation induction time is the time over which a system can withstand supersaturation, constant or increasing[20], before nucleation occurs. In the context of nucleation studies, accurate nucleation induction time measurement has always been difficult to achieve. The main experimental difficulty comes from the stochastic aspect of the nucleation process: we do not know where, when and how many such events occur. Moreover, the size of the critical nucleus is in the nanometre range, requiring either measurement systems addressing the nanoscale (in-situ electron microscopy[21,22], AFM[23,24], laser confocal microscopy[25]), or highly resolved current measurement (using an external localized DC electric field with a nanoelectrode[26]). Because of these difficulties, such small-scale experiments are not performed routinely and their quantitative relevance is still to be confirmed. Consequently, most experiments address the microscale, for instance using turbidity measurements[27]. However, this is quite a large system compared to the supposed size of critical clusters. The price to pay is that assumptions on the nucleation mechanism have to be

made in order to model both growth of individual nucleated clusters and their possible interactions (like Ostwald ripening) until the crystal can be detected[28,29]. Here, we present experiments in which the statistical approach is guaranteed through the large number of identical crystallisers ( $\mu$ Ds) that can be monitored simultaneously. All  $\mu$ Ds will lead to nucleation of only one crystal[30] and because of the fast growth rate (greater than  $200\mu\text{m s}^{-1}$ [26]), the time required for the newly formed nuclei to grow to a detectable size is negligible with regard to the induction time[31]. Thus, these experiments allow us to measure real nucleation induction times without needing to make assumptions on the nucleation mechanism. In the (ROI,  $\sigma$ , t)-plots, nucleation of a crystal inside the  $\mu$ D is seen through a sudden and large increase in  $\sigma$  (Fig. 2a). In Fig. 3a, we plot the line-by-line CDF of  $t_N$  for the 527 microdroplets of **Array 1**. To take into account each  $\mu$ D individual contraction rate[16], we normalise  $t_N$  relative to this rate:  $t_N$  is divided by  $t_M$ . The line-by-line CDF of normalised nucleation times is shown in Fig. 3b, and across lines we observe a narrow and similar distribution of the measured normalised induction times. Such reproducibility in measurements already represents a step forward in experiments addressing nucleation mechanisms.

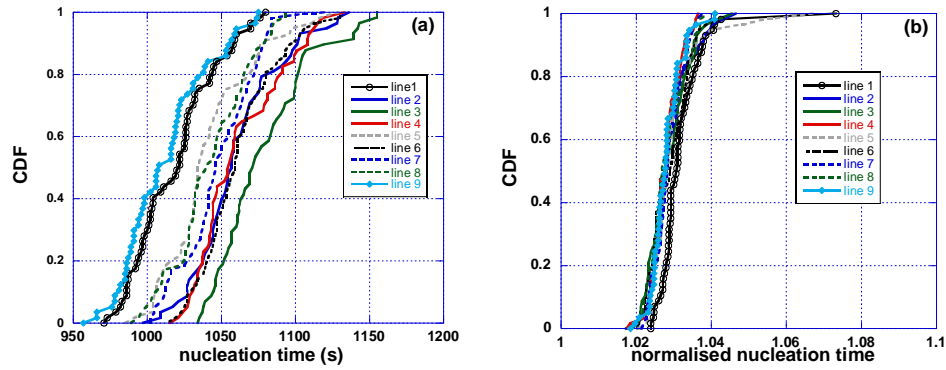


**FIG. 3:** (a) line-by-line CDF of  $t_N$ : for the 527  $\mu$ Ds of **Array 1**, and (b) vs normalised nucleation time line-by-line.

$\mu$ D-contraction can be represented as the sum of two contributions: a vertical water flux toward oil interface with atmosphere, and lateral water fluxes from  $\mu$ D to  $\mu$ D, both responsible for the collective effect. Any change in the experimental conditions (R, D, h, RH) will affect this balance, as demonstrated by **Array 2**. In practice, for **Array 1**  $\mu$ D-contraction, every (ROI,  $\sigma$ , t)-plot presents the same characteristic behaviour: a minimum is reached at  $t_M$  and  $\sigma$  values increase until there is a sudden jump corresponding to crystal nucleation (hereafter these curves are called type 1). For **Array 2**  $\mu$ D-contraction (Fig.S6 and video S2) and  $t_N$ -CDF curve (Fig.S5c), evolution of  $\mu$ Ds seems similar to **Array 1**  $\mu$ Ds. However, a closer look at **Array 2** (ROI,  $\sigma$ , t)-plots shows that some  $\mu$ Ds present (ROI,  $\sigma$ , t)-plots with additional features compared to type 1  $\sigma$ -curve characteristics (Figs. 4 and S7). For two neighbouring (Fig. 4)  $\mu$ Ds, there is a temporal correlation between crystal nucleation in  $\mu$ D#641 (showing type 1  $\sigma$ -curve) and a sudden drop in the  $\sigma$ -curve for  $\mu$ D#640. After this drop,  $\sigma$  reaches a minimum value and then increases again, until there is a sudden jump corresponding to crystal nucleation.  $\sigma$ -curves presenting such a correlated oscillation with nucleation in a neighbouring  $\mu$ D will hereafter be called type 2. The advantage of using (ROI,  $\sigma$ , t)-plots is clear here: both **Array 1** and **Array 2** would be mistakenly considered equivalent without this tool.

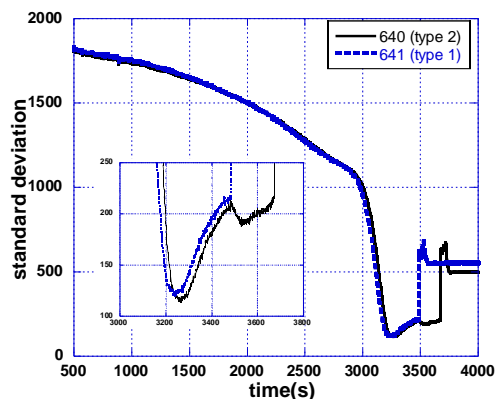


**FIG. 4:** time evolution of standard deviation of neighbouring  $\mu$ Ds 640 and 641 of line 8 of **Array 2**. Insert is a zoom in the nucleation zone.

Collective effects influence  $\mu$ D contraction rates via the instantaneous water concentration field [11,12,17,19], and this work. Moreover, a temporal correlation is observed between two neighbouring  $\mu$ Ds due to nucleation in one  $\mu$ D. When a crystal nucleates in a  $\mu$ D ( $\mu$ D#641, Fig. 4) its rapid growth abruptly decreases the  $\text{Na}^+$  and  $\text{Cl}^-$  concentrations in the droplet. This suddenly increases the chemical potential of water inside the  $\mu$ D (toward the chemical potential of pure water). As a result, there is a sudden increase in water flux from this  $\mu$ D toward its surrounding  $\mu$ Ds when they are close enough ( $\mu$ D#640, Fig. 4). These  $\mu$ Ds without crystals will grow and thereby decrease their solute concentration. As a consequence, both their  $\Delta n$  from surrounding oil and their  $\sigma$  will drop to lower values, as shown by oscillations present on type 2  $\sigma$ -curves.

Now that we have identified this type 2 behaviour, it is clear that it needs to be taken into account when crystallisation is studied. The hypothesis that each  $\mu$ D can be considered independent of the others can now be tested before assuming that a true statistical view of nucleation is obtained. While collective effects during  $\mu$ D contraction can easily be corrected through normalisation relative to  $t_M$  (Fig. 3b), this is not the case for collective effects due to crystal nucleation: the independence required for statistical induction time measurements of contracting  $\mu$ Ds is not respected. Although we expected to find interactions, the mechanism shown here is the opposite of those suggested[10]. In fact, the nucleation of a crystal in a  $\mu$ D does not trigger but delays nucleation in neighbouring  $\mu$ Ds. Moreover, CDF shape is not significantly different regardless of whether nucleation-mediated interactions occur (Fig.S6c) or not (Fig.3a). (ROI,  $\sigma$ , t)-plots appear to be a useful tool both to determine  $\mu$ D independence and to provide data of good quality for nucleation studies.

The method presented in this paper allows us to simultaneously monitor the contraction of a statistically relevant number of  $\mu$ Ds of the same size. The full time-sequence of images is processed to characterise  $\mu$ D dynamics. Every individual  $\mu$ D image is reduced to a scalar standard deviation ( $\sigma$ ), and  $\mu$ D-contraction is monitored using standard-deviation time-evolution plots.

It is shown that this approach not only makes it possible to measure nucleation time but also that  $\mu$ Ds interact via water diffusion. It is also shown that this effect decreases the nucleation rate, contrary to previous findings. Our “ $\sigma$  approach” can be compared to recording an order parameter in phase transition. This makes it ideal for studying the dynamics of systems where images are the primary outputs.

## Acknowledgements

The authors would like to thank Marion Pellen and Marin Jourdan. We thank Marjorie Sweetko for English revision.

## References

- [1] S. Lee and J. Wiener, *Journal of Chemical Education* **88**, 151 (2010).
- [2] M. He, C. Sun, and D. T. Chiu, *Analytical Chemistry* **76**, 1222 (2004).
- [3] D. Brutin, B. Sobac, B. Loquet, and J. Sampaol, *Journal of Fluid Mechanics* **667**, 85 (2011).
- [4] R. Deegan, D., O. Bakajin, T. Dupont, F., G. Huber, S. R. Nagel, and T. Witten, A., *Nature* **389**, 827 (1997).
- [5] V. Dugas, J. Broutin, and E. Souteyrand, *Langmuir* **21**, 9130 (2005).
- [6] K. T. Rodolfa, A. Bruckbauer, D. Zhou, A. I. Schevchuk, Y. E. Korchev, and D. Klenerman, *Nano Letters* **6**, 252 (2006).
- [7] F. De Angelis *et al.*, *Nat Photon* **5**, 682 (2011).
- [8] K. K. B. Hon, L. Li, and I. M. Hutchings, *CIRP Annals - Manufacturing Technology* **57**, 601 (2008).
- [9] P. Laval, A. Crombez, and J.-B. Salmon, *Langmuir* **25**, 1836 (2009).
- [10] A. I. Toldy, A. Z. M. Badruddoza, L. Zheng, T. A. Hatton, R. Gunawan, R. Rajagopalan, and S. A. Khan, *Crystal Growth & Design* **12**, 3977 (2012).
- [11] C. Schäfle, C. Bechinger, B. Rinn, C. David, and P. Leiderer, *Physical Review Letters* **83**, 5302 (1999).
- [12] O. Carrier, N. Shahidzadeh-Bonn, R. Zargar, M. Aytouna, M. Habibi, J. Eggers, and D. Bonn, *Journal of Fluid Mechanics* **798**, 774 (2016).
- [13] Grossier R., Hammadi Z., Morin R., Magnaldo A., and veesler S, *Applied Physics Letters* **98**, 091916 (2011).
- [14] V. Kumar and P. Gupta, *International Journal of Emerging Technology and Advanced Engineering* **2**, 56 (2012).
- [15] Grossier R., Magnaldo A., and veesler S, *J. Crystal Growth* **312**, 487 (2010).
- [16] I. Rodríguez-Ruiz, Z. Hammadi, R. Grossier, J. Gómez-Morales, and S. Veessler, *Langmuir* **29**, 12628 (2013).
- [17] A. J. D. Shaikkea and S. Basu, *Langmuir* **32**, 1309 (2016).
- [18] C. Bourges-Monnier and M. E. R. Shanahan, *Langmuir* **11**, 2820 (1995).
- [19] G. Laghezza, E. Dietrich, J. M. Yeomans, R. Ledesma-Aguilar, E. S. Kooij, H. J. W. Zandvliet, and D. Lohse, *Soft Matter* **12**, 5787 (2016).
- [20] B. Peters, *Journal of Crystal Growth* **317**, 79 (2011).
- [21] B.-S. Lee, G. W. Burr, R. M. Shelby, S. Raoux, C. T. Rettner, S. N. Bogle, K. Darmawikarta, S. G. Bishop, and J. R. Abelson, *Science* **326**, 980 (2009).
- [22] J. Baumgartner, A. Dey, P. H. H. Bomans, C. Le Coadou, P. Fratzl, N. A. J. M. Sommerdijk, and D. Faivre, *Nat Mater* **12**, 310 (2013).
- [23] S. T. Yau and P. G. Vekilov, *Nature* **406**, 494 (2000).
- [24] M. Sleutel, J. Lutsko, A. E. S. Van Driessche, M. A. Durán-Olivencia, and D. Maes, *Nature Communications* **5**, 5598 (2014).
- [25] M. Sleutel and A. E. S. Van Driessche, *Proceedings of the National Academy of Sciences* **111**, E546 (2014).
- [26] Z. Hammadi, R. Grossier, S. Zhang, A. Ikni, N. Candoni, R. Morin, and S. Veessler, *Faraday Discussions* **179**, 489 (2015).
- [27] S. A. Kulkarni, S. S. Kadam, H. Meekes, A. I. Stankiewicz, and J. H. ter Horst, *Crystal Growth & Design* **13**, 2435 (2013).

- [28] Kashchiev D., Verdoes D., and Van Rosmalen G.M., *J. Crystal Growth* **110**, 373 (1991).
- [29] G. M. Maggioni and M. Mazzotti, *Crystal Growth & Design* **17**, 3625 (2017).
- [30] Grossier R. and Veesler S., *Cryst. Growth Des.* **9**, 1917 (2009).
- [31] R. Grossier, Z. Hammadi, R. Morin, and S. Veesler, *Physical Review Letters* **107**, 025504 (2011).

Supplemental Material for:  
**An order parameter to probe microdroplet dynamics**

R. Grossier, V. Tishkova, R. Morin, and S. Veessler  
Centre Interdisciplinaire de Nanoscience de Marseille  
CINaM - CNRS, Aix-Marseille Université  
Campus de Luminy, Case 913, F-13288 Marseille Cedex 09, France  
Phone : 336 6292 2866, Fax : 334 9141 8916, [grossier@cinam.univ-mrs.fr](mailto:grossier@cinam.univ-mrs.fr);  
[veessler@cinam.univ-mrs.fr](mailto:veessler@cinam.univ-mrs.fr)

**Microdroplet generation and monitoring**

Arrays of sessile[1]  $\mu$ Ds are generated by a microinjector (Femtojet, Eppendorf) on an oil-covered 18mm-diameter glass coverslip treated so as to obtain a surface preventing  $\mu$ Ds from spreading and coalescing. Briefly, glass coverslips are spin-coated at 4000rpm for 1min (SPIN 150, SPS) with 4%-950K PMMA (All Resist ARP 679.04) annealed 10 min at 170°C and inserted into a home-made aluminum cell (Fig. S1a). The glass coverslip are then covered with DMS oil ( Polydimethylsiloxane, trimethylsiloxy terminated, M.W. 1250, 10 cSt, refractive index 1.3990 - AlfaAesar) (Fig. S1b) before  $\mu$ D generation.

Both  $\mu$ D generation and subsequent contraction are observed under a transmission optical microscope (Zeiss Axio Observer D1 equipped with an ANDOR neo sCMOS camera) where 16bit images are taken at a 1Hz frequency.

**Array 1 and 2**

For the two  $\mu$ D arrays presented in this paper, both were prepared under common conditions: -injected solution of 0.15 M NaCl aqueous solution (0.025 the solubility of NaCl in water at 20°C[2]) and  $\mu$ Ds are covered with 40 $\mu$ L of DMS oil ( $h = 50\mu\text{m}$ ). The only differences are:  
-**Array 1 (Fig.1a)**: RH = 45%, R = 25.1 $\mu\text{m}$ ,  
-**Array 2 (Fig.ab)**: RH = 65%, R = 34.4 $\mu\text{m}$ ,  
with RH the relative humidity % in room atmosphere above DMS oil and R the initial  $\mu$ D radius.

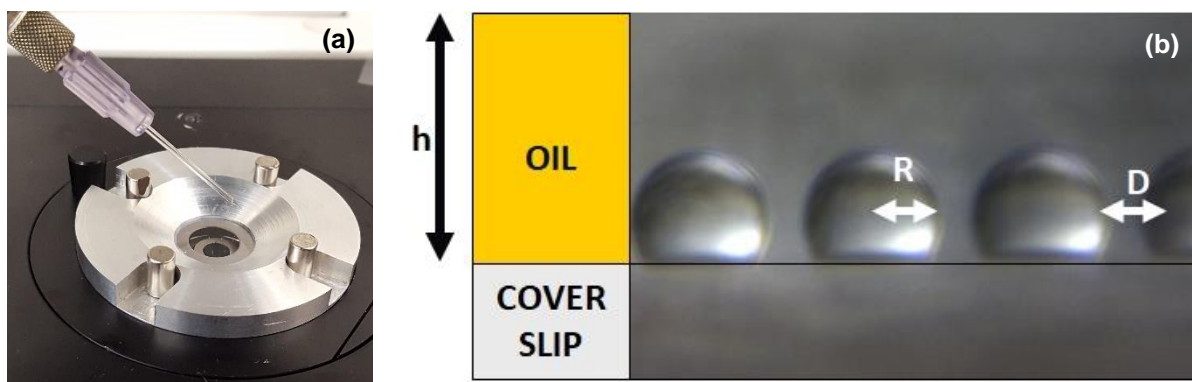


**Fig. S1:** (a) Photo of the home-made aluminum cell for  $\mu$ D deposition storage and monitoring. (b) Side view of  $\mu$ Ds in oil from [3], where R is the  $\mu$ D radius, D the distance between  $\mu$ Ds, and h the oil layer thickness.



**FIG. S2: Array2** immediately after generation, bottom line (line 9) is the most recently generated, 362  $\mu$ Ds with initial droplet radius of  $34.4\mu\text{m} \pm 1.1$  (for line 9), with a volume of 156pL assuming a contact angle of  $130^\circ$ [3]. Outside the field of the image there are lines above line 1 and no line below line 9; their environments are different and therefore their dynamics differ (i.e. contraction rates).



**FIG. S3:** Time sequence showing a line of **Array 1** (line 6 from the top of Fig.1). (a) - (f)  $t=252, 608, 965, 1013, 1034, 1132\text{s}$ .

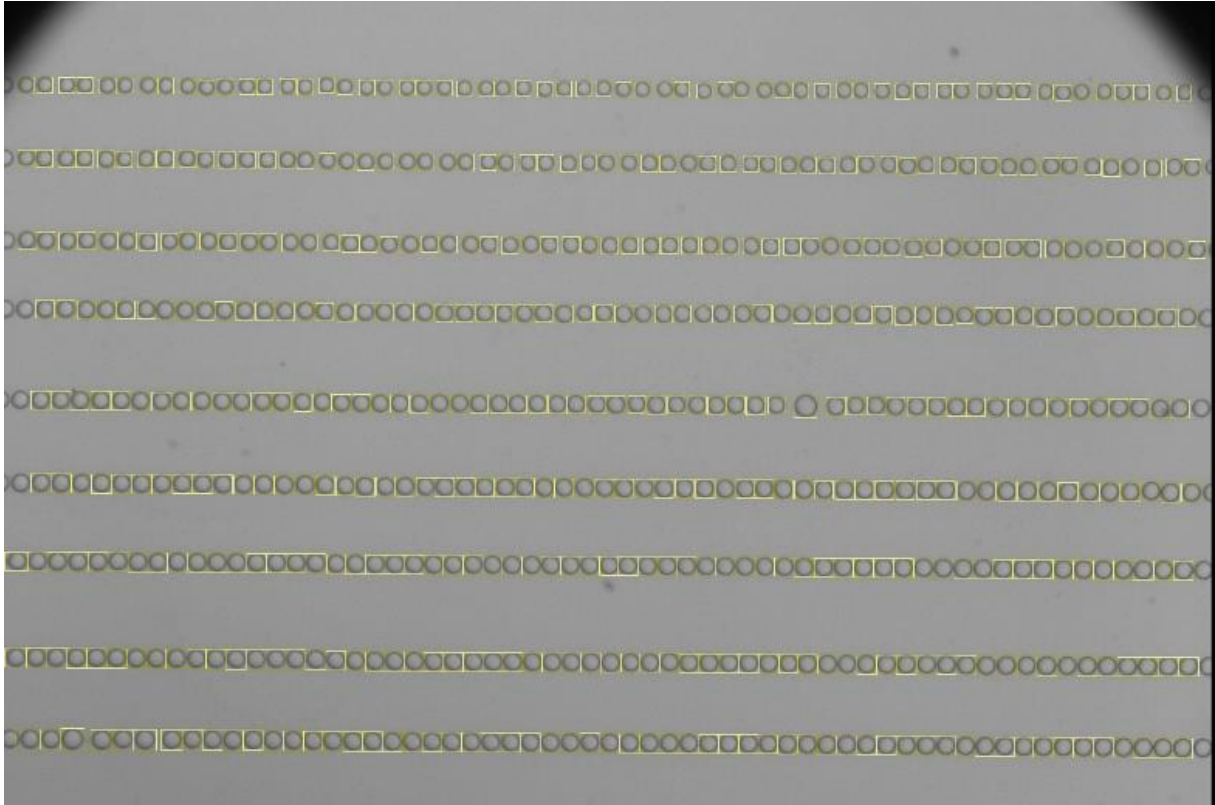


**Fig. S4:**  $\mu$ Ds with the ROI of at  $t=133$ s after the generation of **Array 1**.

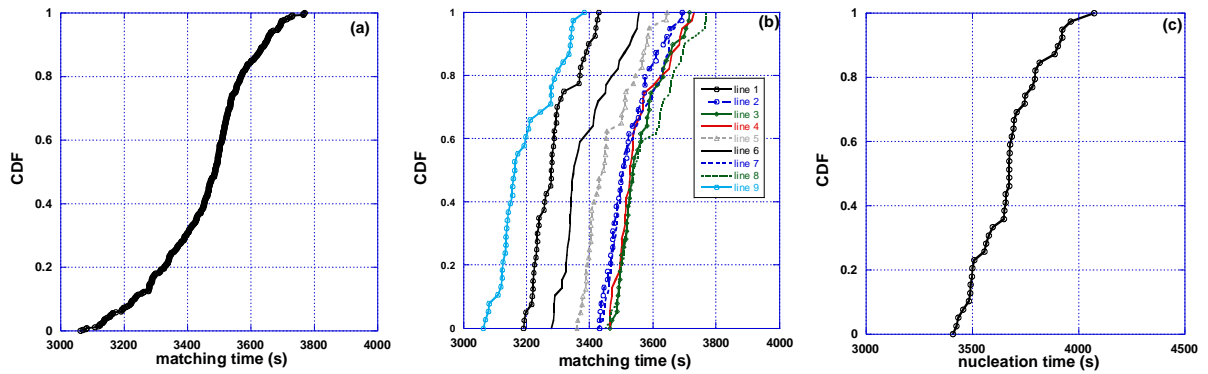


**Fig. S5 :** CDF of  $t_M$  of **Array 2** (a) for the 362  $\mu$ Ds, (b) line-by-line, line 1 to line 9 from top to bottom of fig.2b and (c), CDF of  $t_N$  for the 39  $\mu$ Ds of line 8 (8<sup>th</sup> from the top of Fig.1b)

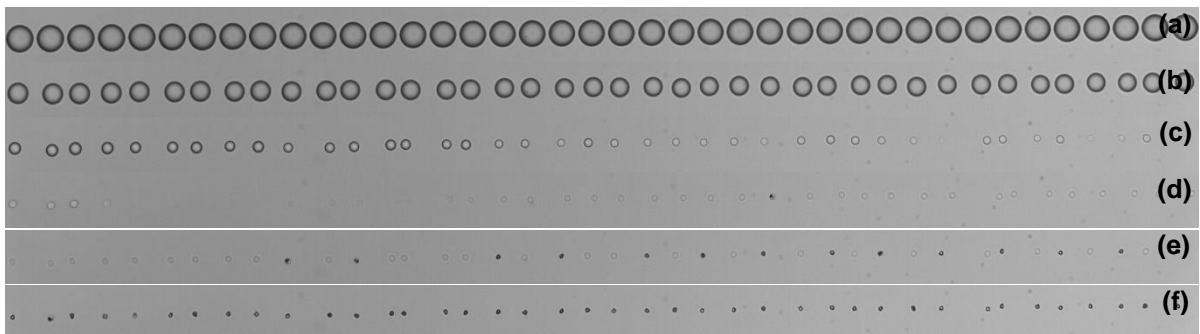


**Fig. S6:** Time sequence showing a line from **Array 2** (8<sup>th</sup> from the top of Fig.2b). (a) – (f)  $t=27, 2029, 3142, 3409, 3597, 4073$ s.

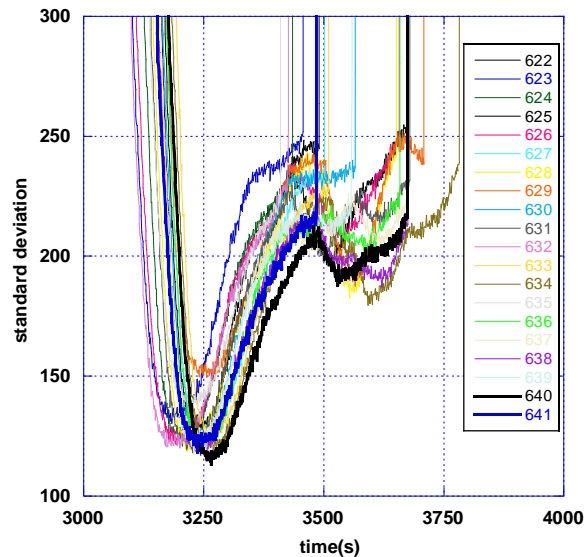


**FIG. S7:** time evolution of standard deviation of neighbouring  $\mu$ Ds 622 to 641 of line 8 of **Array 2** (zoom in the nucleation zone).

**Video S1: Array 1**, injected solution is 0.15 M NaCl aqueous solution,  $\mu$ Ds are covered with 40 $\mu$ L of DMS oil ( $h = 50\mu\text{m}$ ) with an initial droplet radius of 25.1 $\mu\text{m}$ , RH=45%

**Video S2: Array 2**, injected solution is 0.15 M NaCl aqueous solution,  $\mu$ Ds are covered with 40 $\mu$ L of DMS oil ( $h = 50\mu\text{m}$ ) with an initial droplet radius of 34.4 $\mu\text{m}$ , RH=65%

### References

- [1] Grossier R., Hammadi Z., Morin R., Magnaldo A., and veesler S, Applied Physics Letters **98**, 091916 (2011).
- [2] H. Langer and H. Offermann, Journal of Crystal Growth **60**, 389 (1982).
- [3] I. Rodríguez-Ruiz, Z. Hammadi, R. Grossier, J. Gómez-Morales, and S. Veesler, Langmuir **29**, 12628 (2013).